A5: Spectroscopic Ellipsometry
Semiconductor Physics I - Laboratory

Hassan Tanveer - 3735258, Simon Briesenick - 3712933
Experiment conducted on: December 7th, 2020

I. Abstract

We report on the optical response of yttria-stabilized zirconium (YSZ) layers of various thicknesses on sapphire (Al_2O_3) substrates using Ellipsometry in the transparent region. We found that (Ψ, Δ) for various angles of incidence agreed well with the theoretical models presented. Additionally, the dielectric function of $AlGaAs$ of unknown stoichiometry was parametrized using different model dielectric functions (MDF) and the behaviour was related to electronic transitions at the critical points (CP) in the Brillouin zone. Furthermore, the dielectric function of c-plane oriented ZnO was determined as well as the LO and TO phonon modes. Before presenting the results, we discuss important theoretical concepts needed for interpreting the data.

II. Introduction

A. Theoretical Background

1) Vector waves: Of particular interest are so-called *time-harmonic* plane waves, i.e. electromagnetic waves for which each of the Cartesian components of **E** and **H** are of the form [1]

$$a\cos(\tau+\delta) = \Re\{ae^{-i(\tau+\delta)}\} \tag{1}$$

where $a > 0$ and $\tau = \omega t - \mathbf{k}\cdot\mathbf{r}$. Since **E**, **H** and **k** define a right-handed coordinate system, it is customary in literature to define the z-axis along the **k** direction, such that **E** and **H** only have non-zero transversal components. Considering now only the electric field vector, the coordinates (E_x, E_y) are

$$\begin{cases} E_x = a_1\cos(\tau+\delta_x), \\ E_y = a_2\cos(\tau+\delta_y). \end{cases} \tag{2}$$

(a) *Elliptic polarization*:
From eq. (2) it can be shown that the two electric field components obey the equation for a conic, more specifically that of an ellipse:

$$\left(\frac{E_x}{a_1}\right)^2 + \left(\frac{E_y}{a_2}\right)^2 - 2\frac{E_x}{a_1}\frac{E_y}{a_2}\cos\delta = \sin^2\delta, \tag{3}$$

where the phase angle

$$\delta = \delta_y - \delta_x \tag{4}$$

is defined for the range $-\pi < \delta \leq \pi$. In general, the principal axes of the ellipse will not be aligned with the x- and y-axis. Instead, they will be rotated by some angle Ψ, such that one can perform a coordinate transformation to a new set of coordinates x' and y' such that eqn. (2) will be diagonalized to:

$$\left(\frac{E_{x'}}{a}\right)^2 + \left(\frac{E_{y'}}{b}\right)^2 = 1 \tag{5}$$

where a and b are the principal axes of the ellipse. The sense of revolution of the electrical field vector **E** is given by the sign of $\sin\delta$. When $\sin\delta < 0$, the direction of propagation is counter-clockwise and vice versa for $\sin\delta > 0$. However, the phase angle is dependant on the particular set of coordinate axes.

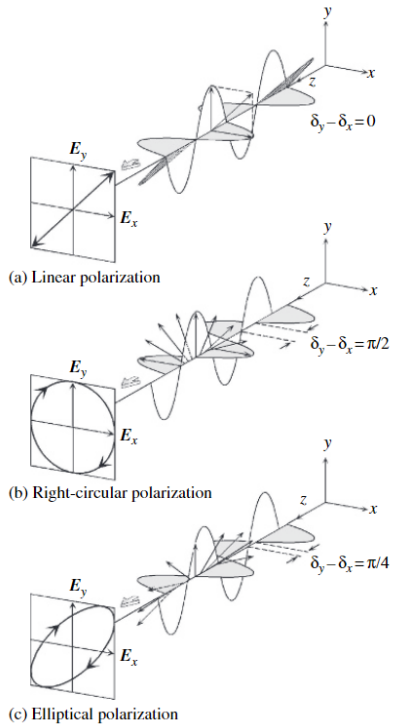

Fig. 1: Polarization states of light, from [2] p.51

(b) *Linear and circular polarization:*
The two most important cases for the polarization ellipse are those, where the ellipse degenerates onto a line or into a circle. The ellipse will reduce to a line, when

$$\delta = \delta_y - \delta_x = m\pi \tag{6}$$

where m can be either 0 or 1. For in this case, the general result, eqn. (2) will simplify to

$$\frac{E_y}{E_y} = (-1)^m \frac{a_1}{a_2 b}. \tag{7}$$

2) Light reflection from boundaries: It is a well-known result from Maxwell's theory that upon reflection of an interface belonging to an isotropic medium, the polarization state of light will change according to the Fresnel equations. They can be given in dependence of the angle of incidence θ_1 and the angle of refraction θ_2

$$r_p = \frac{\tilde{n}_2 \cos\theta_1 - \tilde{n}_1 \cos\theta_2}{\tilde{n}_2 \cos\theta_1 + \tilde{n}_1 \cos\theta_2} \tag{8}$$

$$r_s = \frac{\tilde{n}_1 \cos\theta_1 - \tilde{n}_2 \cos\theta_2}{\tilde{n}_1 \cos\theta_1 + \tilde{n}_2 \cos\theta_2} \tag{9}$$

Subsequently, the reflectivity R is defined as

$$R_i = |r_i|^2 \tag{10}$$

where $i = s, p$, depending on the polarization. There is a special angle, the Brewster angle θ_B, for which the reflected light will be entirely s-polarized. From the reflection coefficient r_p it can be determined to be

$$\theta_B = \arctan \frac{\tilde{n}_2}{\tilde{n}_1}. \tag{11}$$

In analogy, in multi-layered systems a so-called *pseudo*-Brewster angle can often be found for which $|r_p|$ reaches a minimum. In Ellipsometry, one usually measures close to this angle, since the relative changes in the reflectivities are amplified.

3) Dielectric Response of Matter: In general, the response of a material to electromagnetic radiation signal is very complex. In Linear Optics, the assumption is made, that the principal relation between polarization $\mathbf{P}$ and electric field $\mathbf{E}$ can be reasonably well approximated by truncating an expansion of $\mathbf{P}(\mathbf{E})$ in a power series in terms of $\mathbf{E}$ after the linear term [3]

$$\mathbf{P} = \epsilon_0 \chi \mathbf{E} \tag{12}$$

or equivalently

$$\mathbf{D} = \epsilon_0 (1 + \chi)\mathbf{E} = \epsilon_0 \epsilon \mathbf{E}. \tag{13}$$

The quantities χ and ϵ are called the tensors of the susceptibility and the dielectric function, respectively. Both are dependent on the frequency ω and on the wave-vector $\mathbf{k}$ and are in general complex in nature, as shown for ϵ.

$$\epsilon(\omega, \mathbf{k}) = \epsilon_1(\omega, \mathbf{k}) + i\epsilon_2(\omega, \mathbf{k}). \tag{14}$$

The frequency dependence is dominant and the $\mathbf{k}$ is usually dropped in the notation only to be recovered in connection to spatial dispersion [3], which will not be discussed for this report. The tensor of the dielectric function is related to the (complex) refractive index $\tilde{n}$ by

$$\tilde{n}(\omega) = n(\omega) + i\kappa(\omega) = \sqrt{\epsilon(\omega)} \tag{15}$$

where n is the *traditional* refractive index and κ is the extinction coefficient. It follows that

$$\epsilon_1 = n^2 - \kappa^2 \tag{16}$$

$$\epsilon_2 = 2n\kappa \tag{17}$$

where the real and imaginary part of the dielectric function are connected by the Kramers-Kronig relations (KKR)

$$\epsilon_1 = 1 + \frac{2}{\pi} P \int_0^\infty \frac{\epsilon_2(\omega')}{\omega'^2 - \omega^2} d\omega' \tag{18}$$

$$\epsilon_2 = -\frac{2\omega}{\pi} P \int_0^\infty \frac{\epsilon_2(\omega')}{\omega'^2 - \omega^2} d\omega' \tag{19}$$

and P being the Cauchy principal value.

The pseudo-DF is defined as

$$\langle \epsilon \rangle = \left[\left(\frac{1-\rho}{1+\rho} \right)^2 \sin^2\theta + \cos^2\theta \right] \tan^2\theta \tag{20}$$

but will only yield an accurate DF for a perfect substrate (i.e. a semi-infinite, isotropic bulk crystal without surface roughness or contamination)

When the dielectric function of a material is not known, it is necessary to implement models. In accordance to the optical response of the investigated material, one or several model dielectric functions (MDF) need to be chosen. There is a huge variety of dielectric function models. The ones necessary for this analysis are summarized in Table I.

In general, one can write for the MDF

$$\epsilon^{MDF}(E) = \epsilon_\infty + \sum_{j=1}^{N} \epsilon_j(E). \tag{21}$$

Hence, in general, there are N energy-dependant contributions to the polarization of the material that correspond to electronic transitions, phonon resonances or free charge carriers. ϵ_∞ is the background dielectric constant accounting for contributions outside the considered spectral range.

4) Symmetry Considerations for the dielectric tensor: The dielectric tensor is in general a tensor with six independent components

$$\epsilon = \begin{pmatrix} \epsilon_{xx} & \epsilon_{xy} & \epsilon_{xz} \\ \epsilon_{xy} & \epsilon_{yy} & \epsilon_{yz} \\ \epsilon_{xz} & \epsilon_{yz} & \epsilon_{zz} \end{pmatrix} \tag{22}$$

However, there is always a transformation that leaves the ellipsoid

$$\sum_{i,j}^{3} \epsilon_{ij} x_i x_j = const. \tag{23}$$

associated with the tensor to its principal axes. In this representation all of the off-diagonal entries of eqn. 22 vanish. Depending on the symmetries of the investigated material, the number of independent components can be reduced further [1]

(a) Optically isotropic materials, i.e. materials in which three mutually orthogonal crystallographically-equivalent directions may be chosen, such as the case for cubic semiconductors (like YSZ). In this case the dielectric tensor reduces to a constant $\epsilon_{xx} = \epsilon_{yy} = \epsilon_{zz} = \epsilon$.

TABLE I

Dielectric function models		
Model Type	**Functional Form**	**Description**
Lorentz Oscillator	$\epsilon(E) = \frac{A}{E^2_{\text{Lorentz}} - E^2 - i\Gamma_{\text{Lorentz}} E}$.	Semiclassical model for transitions with energy E_{Lorentz} and damping Γ_{Lorentz}. Usually used for high energy or excitonic transitions.
Transitions at the M_0-CP	$\epsilon(E) = A_0\sqrt{E_0}\frac{2 - \sqrt{1+\frac{E+i\Gamma_0}{E_0}} - \sqrt{1-\frac{E+i\Gamma_0}{E_0}}}{(E+i\Gamma_0)^2}$.	With E_0, Γ_0 and A_0 describing the energy, damping and amplitude of the transition, respectively. The transitions described by this model occur at the Γ point. Hence, the fundamental absorption and the split-off valence to conduction band transitions are contributing.
Transitions at the M_1-CP	$\epsilon(E) = -\frac{A_1 E_1^2}{(E+i\Gamma_1)^2}\ln\left(\frac{E_1^2-(E+i\Gamma_1)^2}{E_1^2}\right)$	With the constants as above for the M_0 CP. In cubic $III-V$ semiconductors, the effective mass tensor shows large anisotropy at the L point. The effective mass ellipsoid is distorted strongly, such that the 3D CP can be treated as a 2D CP.
Pole Function	$\epsilon(E) = \frac{A E^{\text{Pol}}}{E^{\text{Pol}} - E}$	Transitions outside the considered spectral range contribute to ϵ_1 and are generally modelled by a constant background dielectric constant (see eqn. 21) or a pole function.
Harmonic Oscillator with Lorentzian Broadening	$\epsilon(E) = \epsilon_\infty \frac{E^2_{LO} - E^2 - i\Gamma E}{E^2_{TO} - E^2 - i\Gamma E}$	In the IR region, the DF is dominated by vibrational modes (phonon modes). Individual contributions need to be multiplied (not summed).

(b) Crystals for which two or more crystallographically-equivalent directions may be chosen in one plane. Trigonal, hexagonal and tetragonal systems belong to this group. One speaks of uniaxial systems with two ordinary (o) and one extraordinary (e) axes (customarily the z-axis) $\epsilon_{xx} = \epsilon_{yy} \neq \epsilon_{zz}$. Furthermore, from the index ellipsoid, the following relation may be found for waves travelling at an angle θ with the optic (z-) axis in uniaxial crystals [4]

$$\frac{1}{n^2(\theta)} = \frac{\cos^2\theta}{n_o^2} + \frac{\sin^2\theta}{n_e^2}. \tag{24}$$

(c) Crystals, where no two mutually crystallographically-equivalent directions may be chosen, so-called biaxial crystals make up the last group, but they won't be of importance for this report and are only listed for completeness. Crystal systems associated as biaxial are the orthorhombic, monoclinic and triclinic systems.

5) Ellipsometry: After reflecting from an interface, the polarization state of light will have changed and is in general in an elliptical polarization state. The p- and s- polarizations of the incident light experience different changes in amplitude and phase upon reflection. In Ellipsometry, the two values (Ψ, Δ) express this change - they represent the amplitude ratio and the phase difference between p- and s-polarizations, respectively. They are hence defined by the ratio of the two (complex) reflection coefficients r_p and r_s

$$\rho = \frac{r_p}{r_s} = \tan\Psi\exp(i\Delta). \tag{25}$$

More specifically,

$$\Psi = \arctan\left(\frac{R_p}{R_s}\right)^{1/2} \tag{26}$$

and

$$\Delta = \delta_p - \delta_s. \tag{27}$$

6) Ψ and Δ in transparent films: For structures like ambient/thin film/substrate (see Fig. 2), eqn. 25 can be expressed as [2]

$$\rho = \frac{r_p}{r_s} = \frac{\left(\frac{r_{01,p}+r_{12,p}\exp(-2i\beta)}{1+r_{01,p}r_{12,p}\exp(-2i\beta)}\right)}{\left(\frac{r_{01,s}+r_{12,s}\exp(-2i\beta)}{1+r_{01,s}r_{12,s}\exp(-2i\beta)}\right)} \tag{28}$$

with $\beta = 2\pi n_1\cos\theta_1/\lambda$ being the phase accumulated by light by travelling through the film and r_{ij} being the reflection coefficients between layer i and layer j as defined by eqn. 8 and 9 with real refractive indices. For the primary and secondary beams to show constructive interference the phase difference between them needs to vanish:

$$\beta = 2\pi m \tag{29}$$

with $m = 1, 2, 3, ...$ From which follows

$$\frac{2dn_1\cos\theta_1}{\lambda} = m \tag{30}$$

An alternative expression in terms of the photon energy can also derived by replacing λ

$$E = \frac{mhc}{2dn_1\cos\theta_1}. \tag{31}$$

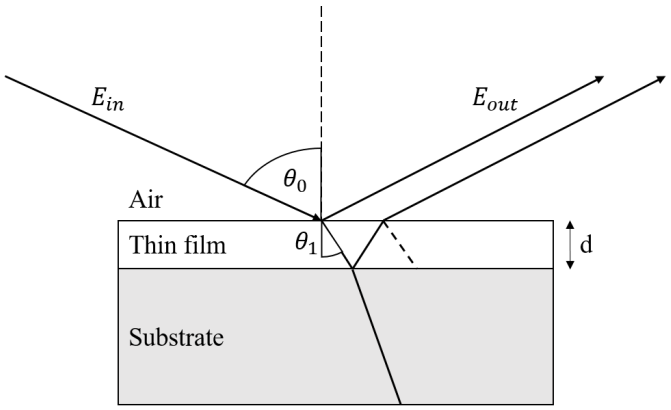

Fig. 2: Illustration of thin film on top of substrate

Hence, in transparent films, the interference effect is periodic in the photon energy with a constant period. The refractive index in transparent isotropic media is modelled using the Cauchy Ansatz

$$n(E) = A + BE^2 + CE^4 \tag{32}$$

with A, B and C being the Cauchy coefficients.

The reflection coefficients R_s and R_p are hence dependent on the energy. A computational model showing the reflectivities for a structure as shown in Fig. 2 can be seen in Fig. 3. The real refractive indices were taken to be constant and are typical values for the investigated materials YSZ [5] and sapphire [6], albeit that the refractive indices are in reality (weakly) dependant on the energy for the range in question. Hence, the showcased curves can only indicate a general trend and the extrema positions should not be taken to be exact.

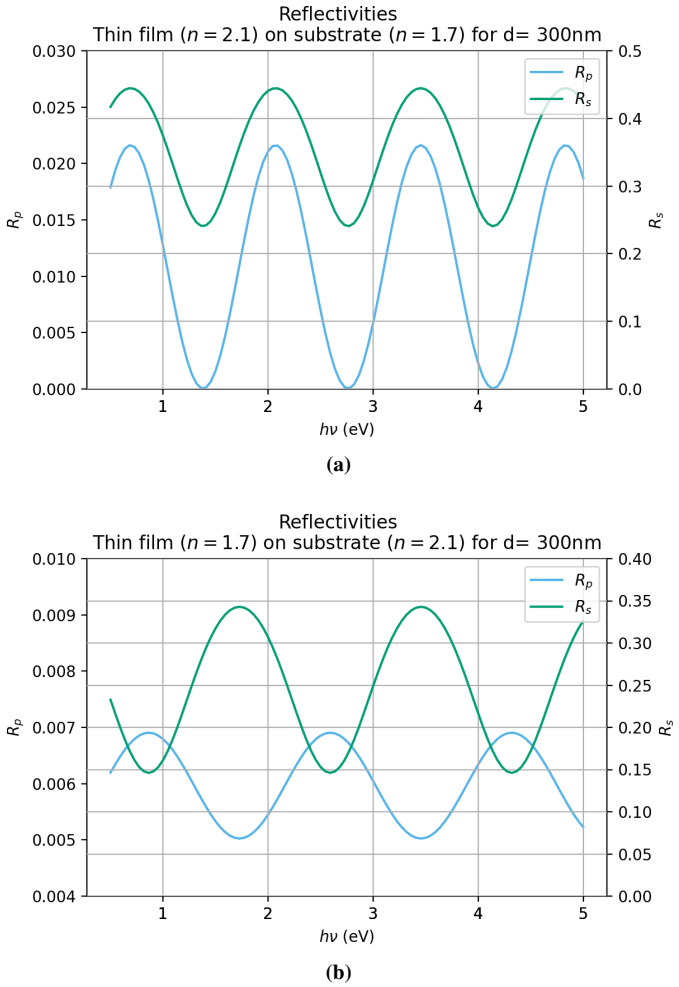

Fig. 3: In this model, constant refractive indices for the thin film and the substrate and a constant incidence angle of $\theta = 60°$ were assumed. In the above case, the refractive index is greater then that of the substrate and vice versa for below. It can be seen that the Extrema of R_p and R_s align in the prior case while anti-aligning in the latter one.

B. Experimental Setup

All data presented in this report was recorded with either the $M2000$ or the IR-VASE ellipsometers, both built by the J.A. Woollam company. The $M2000$ was operated in the rotating compensator ellipsometer configuration, while the infrared ellipsometer was operated in the variable angle spectroscopic ellipsometer configuration. A schematic of the measurement setup is shown below.

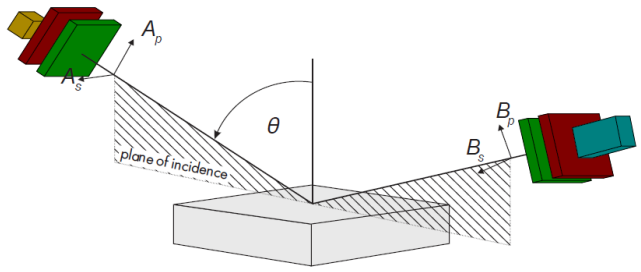

Fig. 4: Schematics of the measurement configuration. The functionality of the individual, colored components is described in the text. Graphic from [8].

The light source (yellow) emits light that is first passed through a polarizer (red) and a $\lambda/4$-plate (green). After reflecting from the surface, the electric field components B pass through a second compensator and polarizer to be detected by a detector (blue).

The data we present here was plotted using *Python* and obtained from the data acquisition program *WVASE*.

C. Material Information

Yttria-stabilized zirconia (YSZ) layers with varying thicknesses were deposited on sapphire substrates (Al_2O_3) by pulsed laser deposition. According to [9] [10], YSZ typically grows in a cubic structure and is transparent for a relatively large region from the near-infrared (NIR) to the ultraviolet (UV). The optical band gap of YSZ is around $E_g = 5.7eV$. $Al_xGa_{1-x}As$ is, dependant on the mole fraction x a direct or indirect semiconductor. In UV-Vis-NIR ellipsometry, transitions at the Γ and L points, as well as higher energetic transitions at the X point can usually be observed. The

transition energies (in eV) observed in this report are [7]

$$E_0 = 1.425 + 1.115x + 0.37x^2 \quad (33)$$
$$E_0 + \Delta_0 = 1.765 + 1.115x + 0.37x^2 \quad (34)$$
$$E_1 = 2.925 + 0.97x \quad (35)$$
$$E_1 + \Delta_1 = 3.155 + 0.945x. \quad (36)$$

where the energies correspond to the transitions marked in Fig. 5. Lastly, we report on the IR dielectric tensor components $\epsilon_{\parallel,\perp}$ of a commercially obtained c-plane oriented ZnO single crystal in wurtzite structure.

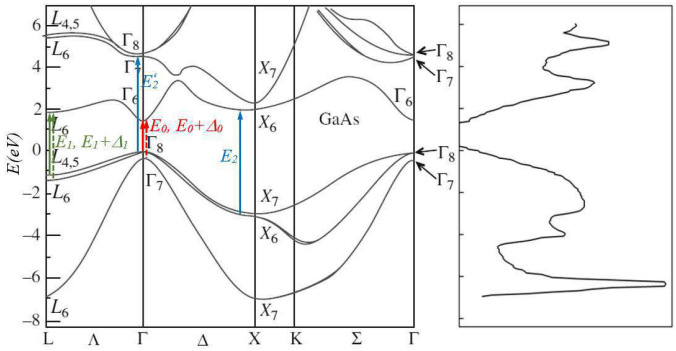

Fig. 5: Band structure (left) and electronic density of states (right) of $GaAs$. From [8].

III. Results and Discussion

A. Al_2O_3 substrate

For various fixed angles of incidence, Ψ and Δ are shown in Fig. 6. For both quantities the position of the Brewster angle largely determines the shape of the curves shown. For each angle of incidence θ, Ψ can be seen to stay more or less constant over the entire energy range, reaching its lowest value for $\theta = 60°$, close to the theoretical Brewster angle θ_B. After reflecting from the interface, the p and s polarization states experience different phase shifts. As discussed above, the s-polarized light, always experiences a phase shift of π, independent of θ. The p-polarized light on the other hand experiences no phase shift for $\theta < \theta_B$, but a phase shift of π for $\theta > \theta_B$. Hence, the relative phase between the two polarization components remains at $180°$ for low angles and reaches $0°$, once the Brewster angle is crossed, with some sharp transition between the two extremes.

The influence of the Brewster angle can also be observed in Fig. 7 for which the photon energy was fixed ($E \cong 2eV$) and the angle of incidence varied.

B. YSZ layers on Al_2O_3

For fixed energy, $E = 2eV$, and layer thickness $d = 100nm$ (see Fig. 8), the variation of (Ψ, Δ) can be explained as follows. Ψ, being defined by eqn. 26, takes on a value of $45°$ since at normal incidence, there is no distinction of the $s-$ and $p-$ polarized waves, i.e. $R_p = R_s$. Increasing the angle of incidence leads to the two components becoming non-degenerate, more specifically $R_p < R_s$, hence Ψ decreases until the (pseudo-)Brewster angle θ_B is reached at about $65°$ where R_p attains a local minimum. After passing through the Brewster angle, R_p increases again for larger angles of incidence and again equals R_s for $\theta \to 90°$. For $\theta < \theta_B$, $\Delta = 180°$. At the Brewster angle, the two polarization components get in phase with a smooth transition from $180°$ to $0°$.

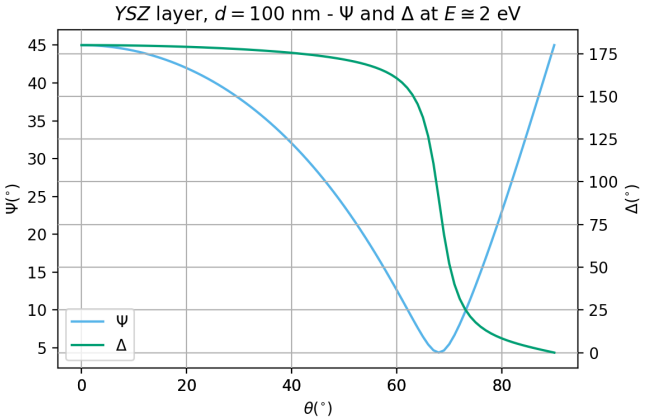

Fig. 8: Variation of (Ψ, Δ) as a function of the incidence angle θ.

For several YSZ layer thicknesses d, the variation of (Ψ, Δ) are shown in Fig. 9. The simulation was run at a fixed angle of incidence of $\theta_0 = 60°$ and plotted for a range of photon energies between 0.5 eV and 3.5 eV. The oscillations of Ψ and Δ are indeed also attributable to the interference effect described in eqn. 31. Clearly, the phase shift

Qualitatively, the oscillations in Ψ can also be explained by Fig. 3a. Since $\Psi = \arctan(\frac{R_p}{R_s})^{1/2}$, Ψ periodically gets very close to 0 when R_p reaches a local minimum and vice versa for the maxima. Ψ is generally quite low for all layer thicknesses, since the model was implemented close to the Brewster angle. For a layer thickness of $d = 0$nm, Ψ increases steadily because the refractive index of the substrate is actually energy-dependant. Indeed, this shifts the position of the Brewster angle θ_B and consequently Ψ changes. It can be seen that for all layer thicknesses, the extrema amplitudes shift to larger values in correspondence to this effect.

In the absence of a transparent YSZ layer, the relative phase shift Δ between the two polarization components stays constant at $180°$. As the interaction occurs below the Brewster angle, the p-polarization experiences no phase change, while the s-polarization suffers a phase shift of π upon reflection from the substrate interface. As the layer thickness increases, the

After having discussed the models, we can make the following qualitative observations about the experimental results (see Fig. 10). Since the oscillation period in Ψ gets larger from the first of the samples, S966, to the last one, S984, one expects the layer thickness to decrease in the same order. This is indeed what we obtained from the fitting models

$$d_{S966} = (113.01 \pm 0.02)nm,$$
$$d_{S967} = (84.83 \pm 0.02)nm,$$
$$d_{S984} = (39.10 \pm 0.2)nm.$$

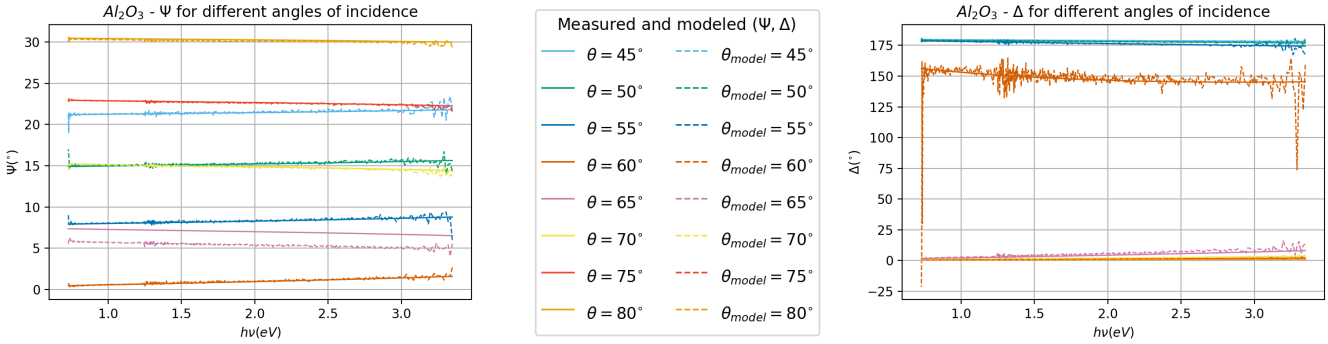

(a) **(b)**

Fig. 6: Sapphire Substrate - (Ψ, Δ)

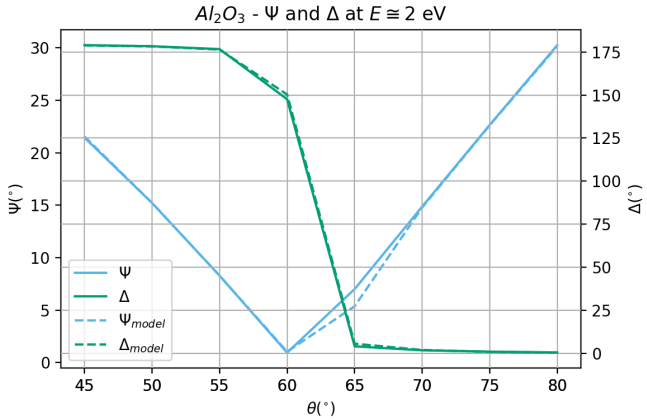

Fig. 7: Sapphire Substrate - (Ψ, Δ) for a fixed energy.

A multi-sample fit is of particular usefulness here, since the optical constants for each sample should be identical. Furthermore, the top surface was modelled to have a certain roughness from the deposition process. This explains the fuzziness in the models for Ψ that becomes increasingly important for higher photon energies $h\nu$.

C. $Al_xGa_{1-x}As$ layer on GaAs substrate

The stoichiometry and layer thickness of the deposited layer was determined by fitting (Ψ, Δ) to the spectral range for varying angles of incidence (Fig. 11). Again, we observe layer thickness oscillations with decreasing amplitude in both parameters in the transparent region until around $h\nu = 1.95$ eV. For larger energies, absorption processes dominate. The model fit for the entire spectral range (in *WVASE*) fixed the mole fraction x to $x = 0.36$. Using eqns. 33-36, the transition energies (in eV) can then be determined as

$$E_0 = 1.87, \tag{37}$$
$$E_0 + \Delta_0 = 2.21, \tag{38}$$
$$E_1 = 3.27, \tag{39}$$
$$E_1 + \Delta_1 = 3.50. \tag{40}$$

The layer thickness is $d = (1548.1 \pm 0.2)nm$. The dielectric function for different stoichiometry values x is presented in Fig. 12.

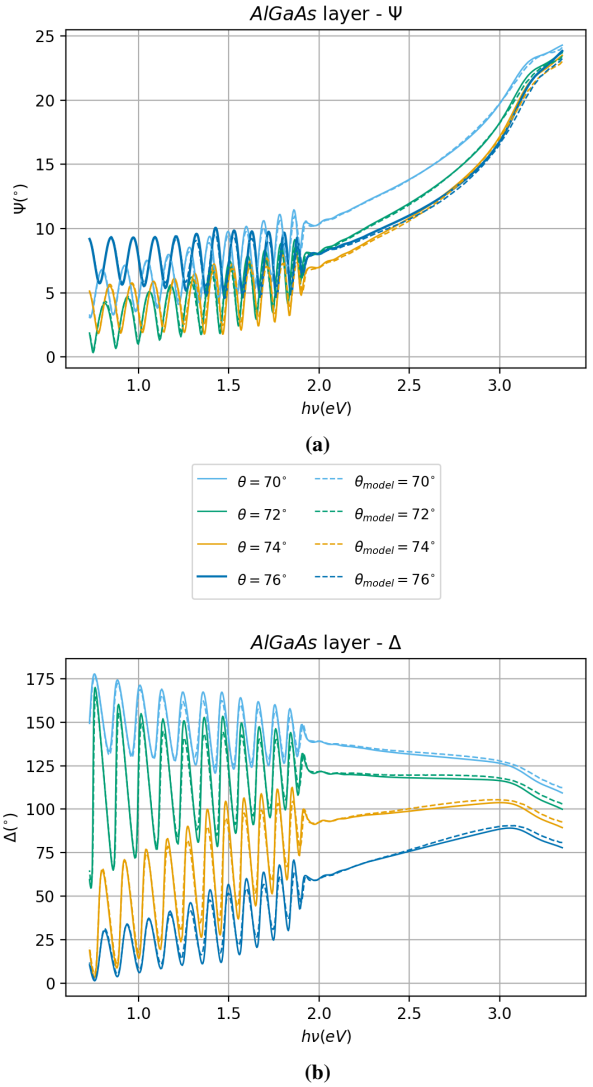

(a)

(b)

Fig. 11: $AlGaAs$ - (Ψ, Δ) and corresponding model fits for the entire range of energies

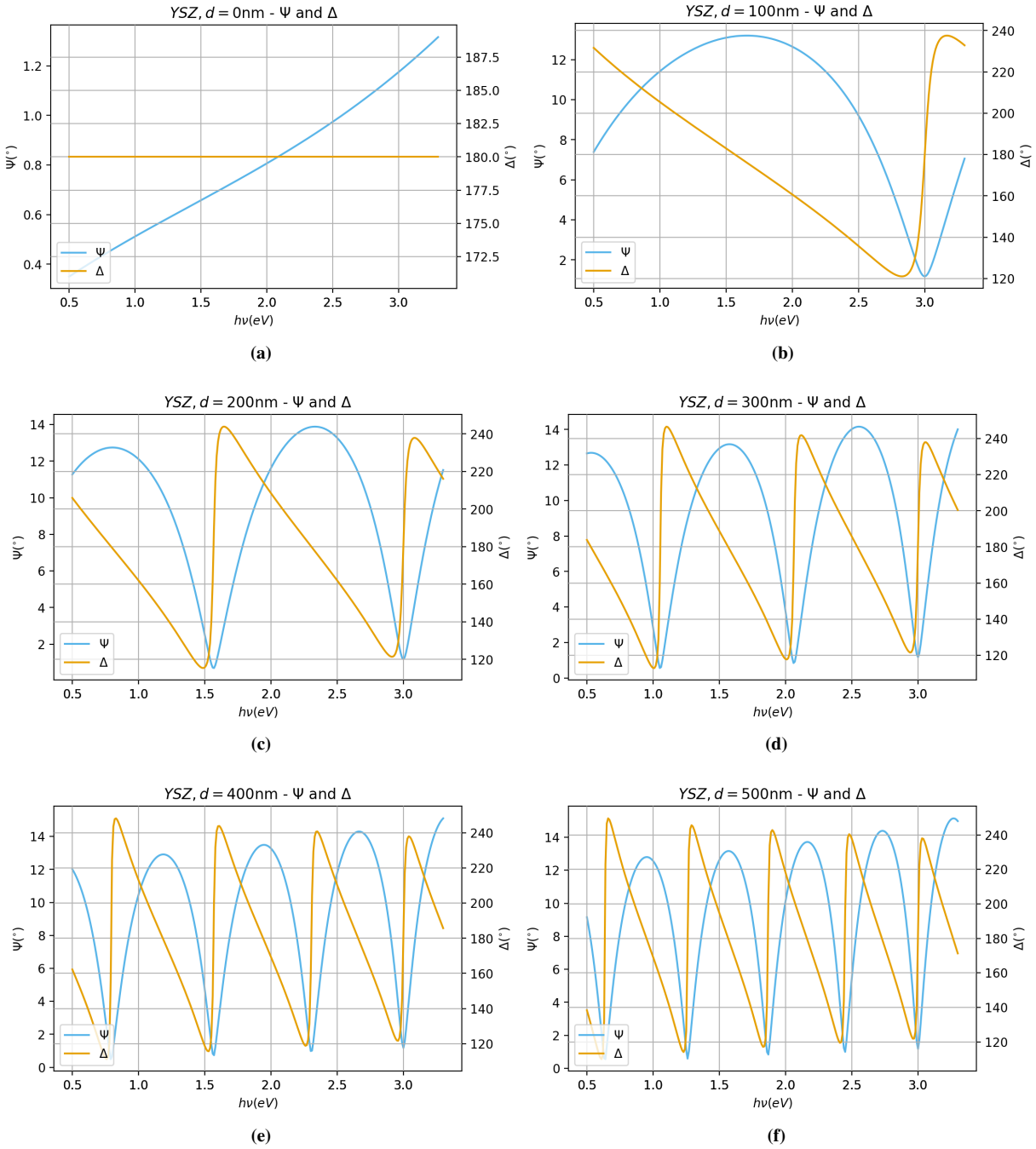

Fig. 9: Dependence of ellipsometric angles on layer thickness in YSZ at an incidence angle of $\theta = 60°$

As expected, the electronic transitions at the critical points (CPs) can be observed in ϵ_2. The observations can be summarized as follows

1) The transition at the M_0 CP from $\Gamma^6 \rightarrow \Gamma^6$, i.e. from the split-off valence band to the conduction band is theoretically possible, but is barely visible to the eye.
2) The onset of absorption shifts to higher energies in accordance to the shift of the transition energies with increasing x.
3) The split-off transitions at the M_1 CP (shoulder to the E_1 peak for ϵ_2) become less pronounced with increasing x.
4) The peak amplitude in ϵ_2 due to transitions at the L point reaches a Minimum for $x \cong 0.5$.

For the given sample, the dielectric function can be seen to follow the same trend (see Fig. 13). Using the above calculated transition energies with associated dielectric function models (Table I) for ϵ_2, we could manually fit the total MDF to the data. The result, Fig. 14, is quite good. Except for intermediate values for $h\nu$ between 2.5 and 3.0eV, the fitted model matches the measured value closely. In this model, the split-off band to conduction band transitions were not included and it is

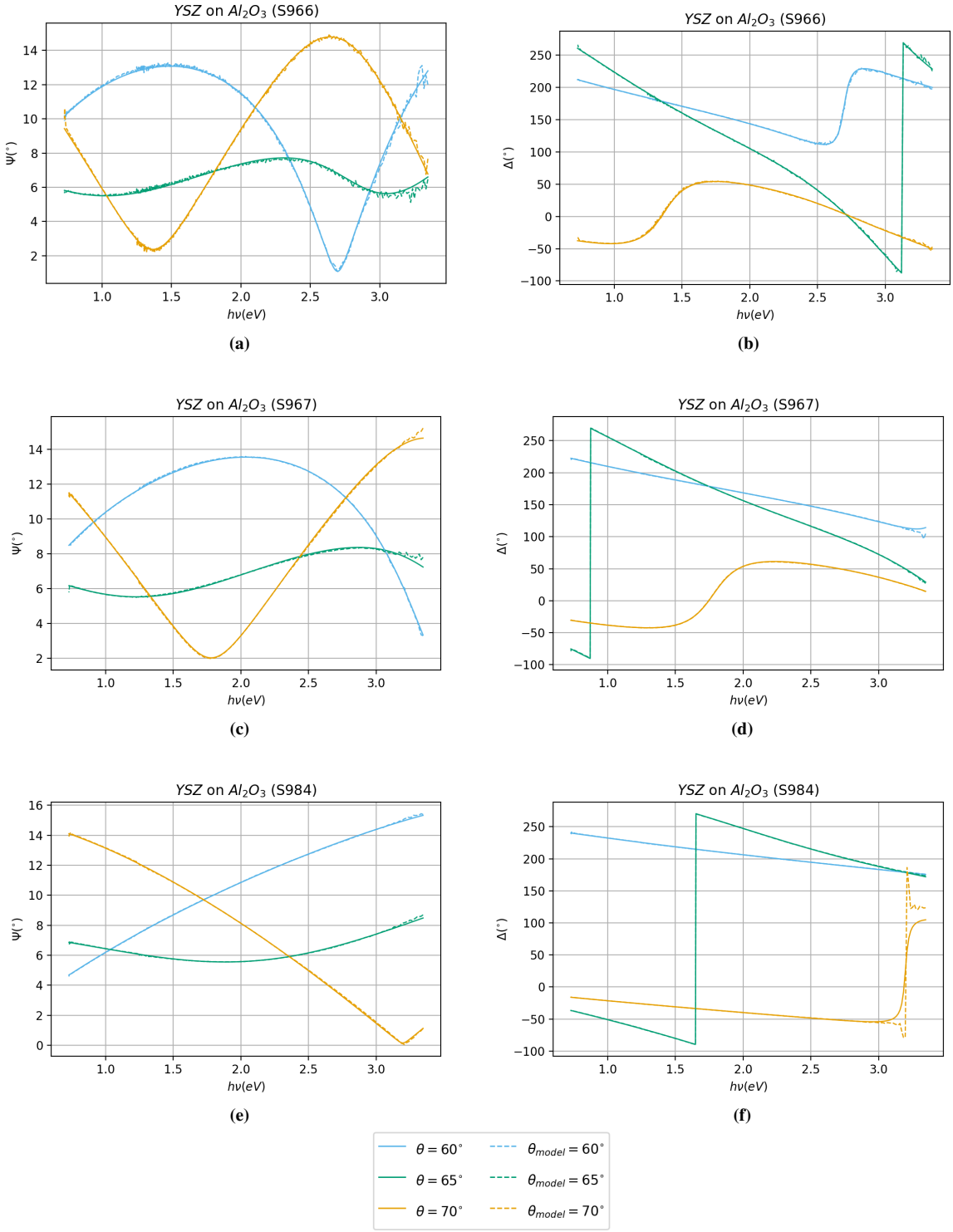

Fig. 10: Measured (Ψ, Δ) for various YSZ thin film samples of unknown thicknesses grown on sapphire substrates.

certainly possible to obtain a qualitatively better fit by implementing a fit model containing those contributions as well. Indeed, transitions with energies corresponding to eqn. 38 could have an important influence in the intermediate region. The fit parameters are given in Table II in accordance with the definitions in Table I. Clearly, the higher order transitions close to the X point, corresponding to transition energies of E_2 between 4.89 and 4.99 eV [7] can not be found in the observed region. They could, however, make important contributions to the behaviour of ϵ_1 due to the KKR.

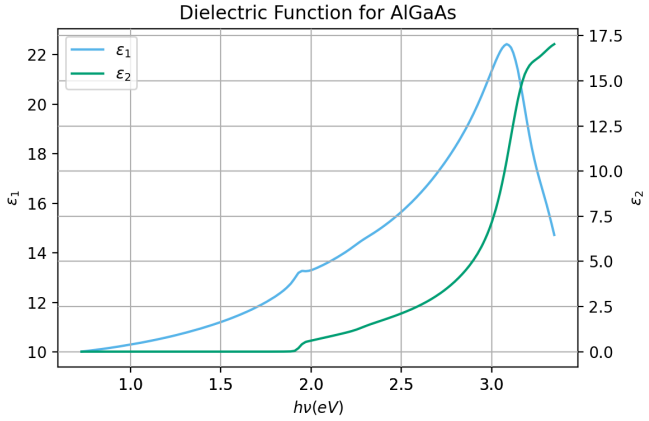

Fig. 13: Real and Imaginary parts of the dielectric function.

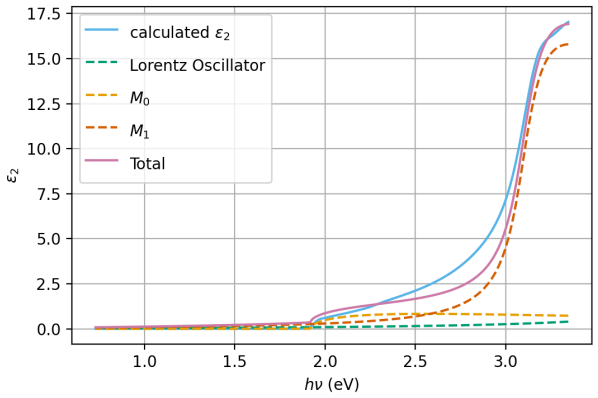

Fig. 14: For this model, three distinct transitions were assumed. However, the influence of higher transitions around $E = 4.93$ eV is almost negligible for the considered range.

TABLE II

MDF - Summary			
Model Type	E (eV)	A	Γ
M_0-CP	1.87	6.8	0.001
M_1-CP	3.27	7	0.1
Lorentz Oscillator	4.93	-	-

D. DF of ZnO

The following discussion is heavily based on a paper published by Ashkenov et. al. [11]. Fig. 15 shows the results for (Ψ, Δ) at a fixed angle of incidence of $\theta = 70°$. It can be interpreted as follows

1) Ψ reaches a roughly constant value of Ψ $45°$ which indicates that the reflectivities for the region in question become identical. Hence, the region can be identified as the bands of total reflection (Reststrahlen bands).
2) In the primitive unit cell of wurtzite ZnO are four basis atoms indicating that there are in total 12 phonon modes, 9 of which are optical phonon modes. At the Γ point in the Brillouin zone, the optical phonon modes can be classified by the irreducible representation [12]
$$\Gamma_{\text{opt}} = 1A_1 + 2B_1 + 1E_1 + 2E_2. \tag{41}$$
The A_1 and E_1 modes are polar, since an oscillating polarization is associated with their motion. Due to Coulomb interaction, both modes split into transverse optical (TO) and longitudinal optical (LO) phonons with different frequencies [12]. The other four modes (the B_1 and E_2 modes) are IR inactive. Total internal reflection occurs between the $E_1(TO)$ and $E_1(LO)$ phonon modes.
3) The small dent in the plateau of Ψ is caused by the loss in p reflectivity at $E_1(LO)$. The cause of this might be due to the A_1 mode displacements being parallel to the c-axis, while the the E_1 mode displacements are perpendicular to the c-axis.
4) The behaviour of Ψ and Δ around $650cm^{-1}$ is explained by the observation that $|\epsilon_{\parallel}|$ and $|\epsilon_{\perp}|$ reach unity for slightly different wave numbers. When $|\epsilon_{\parallel}|$ 1, r_p reaches it's lowest value, and Ψ experiences a minimum. On the other hand, when $|\epsilon_{\perp}|$ 1, r_s reaches it's lowest value and Ψ experiences a maximum.

The dielectric tensor of ZnO has two components, $\epsilon_{\perp}$ and $\epsilon_{\parallel}$. For modelling the DF components in the IR region, the above harmonic oscillator model with Lorentzian broadening was used for both with contributions from A_1 and E_1 modes. The results are shown below. Comparing the obtained DF with those of others [11], we see that the the parallel component of the dielectric function, $\epsilon_{\parallel}$ differs significantly, while $\epsilon_{\perp}$ gives a close match to previously obtained values. Our results are compared with those of others in Table III. The $A_1(TO)$

TABLE III

ZnO - DF Parameters [11]			
$\tilde{\nu}(cm^{-1})$ [phonon mode]	$\tilde{\nu}(cm^{-1})$	ϵ_{∞}	$\Gamma(cm^{-1})$
410 ± 0.3 $[E_1(TO)]$	409.1	3.8 ± 0.2	13.2 ± 0.3
589 ± 0.7 $[E_1(LO)]$	588.3	3.8 ± 0.2	13.2 ± 0.3
350 ± 20 $[A_1(TO)]$	380	3.67 ± 0.05	14.7 ± 0.4
570 ± 0.3 $[A_1(LO)]$	574.5	3.67 ± 0.05	14.7 ± 0.4

phonon mode could only be measured with a large uncertainty. To obtain a more accurate result Raman spectroscopy should be used.

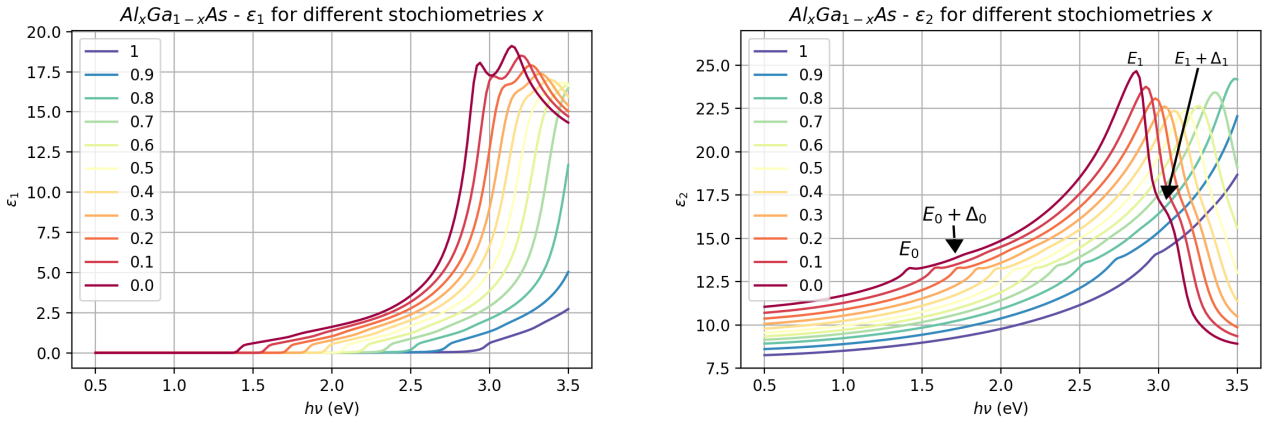

(a) **(b)**

Fig. 12: Dielectric Function $\epsilon = \epsilon_1 + i\epsilon_2$ for different mole fractions x.

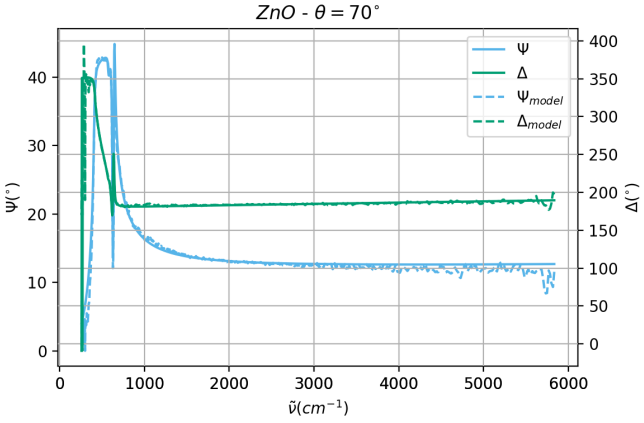

(a)

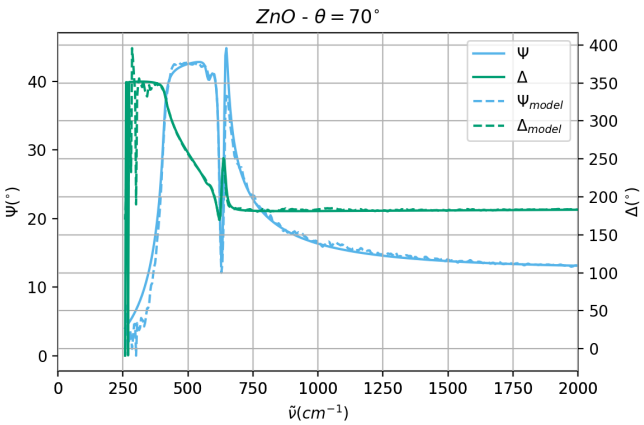

(b)

Fig. 15: (Ψ, Δ) for an angle of incidence of $\theta = 70^\circ$ as a function of the wavenumber $\tilde{\nu}$.

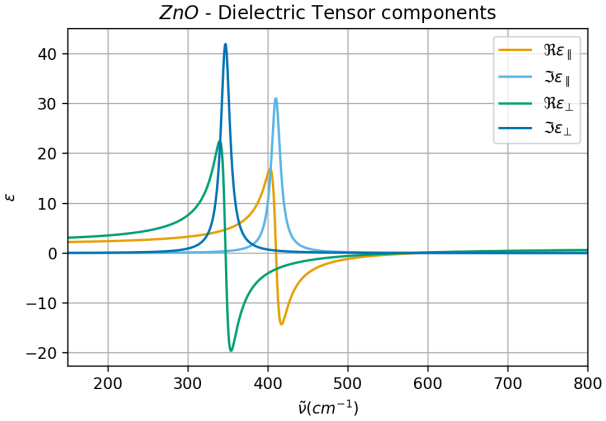

Fig. 16: The dielectric tensor in uniaxial ZnO has two components, $\epsilon_\parallel$ and $\epsilon_\perp$.

REFERENCES

[1] M. Born, E. Wolf, 2011, *Principles of Optics*, 7th edition. Cambridge University Press.

[2] H. Fujiwara, 2003, *Spectroscopic Ellipsometry, Principles and Applications*. John Wiley & Sons, Ltd.

[3] C. Klingshirn, 2012, *Semiconductor Optics*, 4th edition. Springer-Verlag Berlin Heidelberg.

[4] B. Saleh, M. Teich, 1991, *Fundamentals of Photonics*, 1st edition. John Wiley & Sons, Inc.

[5] D. L Wood and K. Nassau, 1982, *Refractive index of cubic zirconia stabilized with yttria*, Appl. Opt. 21, 2978-2981

[6] M. J. Dodge, 1986, "Refractive Index" in *Handbook of Laser Science and Technology, Volume IV, Optical Materials: Part 2*, CRC Press, Boca Raton, p. 30

[7] S. Adachi, Journal of Applied Physics 58, R1 (1985); https://doi.org/10.1063/1.336070

[8] Dr. R. Schmidt-Grund, *A5: Spectroscopic Ellipsometry*, Lab course semiconductor physics

[9] S. Heiroth, R. Ghisleni, T. Lippert, J. Michler, A. Wokaun, *Optical and mechanical properties of amorphous and crystalline yttria-stabilized zirconia thin films prepared by pulsed laser deposition*, Acta Materialia, Volume 59, Issue 6, 2011, P. 2330-2340, ISSN 1359-6454, https://doi.org/10.1016/j.actamat.2010.12.029.

[10] Michael B. Pomfret, Chad Stoltz, Bindu Varughese and Robert A. Walker, *Structural and Compositional Characterization of Yttria-Stabilized Zirconia: Evidence of Surface-Stabilized, Low-Valence Metal Species*, Analytical Chemistry 2005 77 (6), 1791-1795 DOI: 10.1021/ac048600u

[11] N. Ashkenov, B. Mbenkum, C. Bundesmann, V. Riede, M. Lorenz, D. Spemann, E. Kaidashev, A. Kasic, M. Schubert, M. Grundmann, et al.,

Infrared dielectric functions and phonon modes of high-quality zno films, Journal of Applied Physics, Vol. 93, No. 1, pp. 126–133, 2003.

[12] C. Klingshirn, B. Meyer, A. Waag, A. Hoffmann, J. Geurts, 2010, *Zinc Oxide: From Fundamental Properties Towards Novel Applications*, Springer Verlag Berlin Heidelberg.

IV. Appendix

The correlation matrices for fitting (Ψ, Δ) in three different regions of the energy are shown below.

Correlation Matrix

	Thick.1	Alloy.1	Thick.2	ThkUni
Thick.1	1.000	0.913	0.104	0.311
Alloy.1	0.913	1.000	0.150	0.343
Thick.2	0.104	0.150	1.000	0.028
ThkUni	0.311	0.343	0.028	1.000

Fig. 17: Whole spectral range, $d = 1553.3 \pm 0.2$ nm.

Correlation Matrix

	Thick.1	Alloy.1	Thick.2	ThkUni
Thick.1	1.000	0.961	0.028	0.541
Alloy.1	0.961	1.000	0.071	0.562
Thick.2	0.028	0.071	1.000	-0.031
ThkUni	0.541	0.562	-0.031	1.000

Fig. 18: Transparent spectral range, $d = 1549.5 \pm 0.3$ nm.

Correlation Matrix

	Thick.1	Alloy.1	Thick.2	ThkUni
Thick.1	1.000	0.058	0.079	0.036
Alloy.1	0.058	1.000	0.533	0.042
Thick.2	0.079	0.533	1.000	-0.015
ThkUni	0.036	0.042	-0.015	1.000

Fig. 19: Absorbing spectral range, $d = 2482 \pm 15$ nm

For identification purposes,

1) *Thick.1* and *Alloy.1* are thickness and molar fraction x of Aluminium in the $AlGaAs$ layer
2) *Thick.2* is the thickness of the $GaAs$ substrate

If the fit is performed in the absorbing region, the layer thickness is dramatically different to the other two. This is indeed sensible, since the behaviour of Ψ and Δ are mainly determined by reflection at the interface layer. In the transparent region, due to interference, the layer thickness can be determined quite well. If the layer is strongly absorbing, secondary beams are not allowed and there is no Interference, strongly reducing our ability to determine the layer thickness. The Correlation value between the $AlGaAs$ layer thickness and alloy concentration x of > 0.9 in both, the whole spectral and the transparent range, reflects the interdependence of both parameters in the fit model, even though these two parameters are in principle physically completely independent.